

On the HR 4796 A circumstellar disk^{*}

J.C. Augereau¹, A.M. Lagrange¹, D. Mouillet¹, J.C.B. Papaloizou², and P.A. Grorod¹

¹ Laboratoire d'Astrophysique de l'Observatoire de Grenoble, Université J. Fourier / CNRS, B.P. 53, F-38041 Grenoble Cedex 9, France

² Astronomy Unit, School of Mathematical Sciences, Queen Mary and Westfield College, Mile End Road, London E1 4NS, UK

Received 18 December 1998 / Accepted 14 June 1999

Abstract. We investigate in details the properties of the disk surrounding the 8 Myr old star HR 4796 A, one of the few stars bringing precious clues to better understand the scenario which lead to planetary system formation. We propose a model able to reproduce all the available observations: the full spectral energy distribution from the mid-infrared to the millimeter wavelengths, resolved scattered light and thermal emission observations. We show that the circumstellar matter splits into two dust components: a cold annulus, peaked at 70 AU from the star, made of ISM-like grains (amorphous composition, porosity ~ 0.6) larger than $10\ \mu\text{m}$ and a population of hot dust close to the star (at about 9 AU) made of comet-like grains (crystalline composition, porosity ~ 0.97). Both dust populations are highly collisional and the grain size distribution in the cold annulus is found to be cut-off by radiation pressure. At 70 AU, bodies as large as a few meters are required to fit the data leading to a minimum disk mass of a few Earth masses and to a gas to dust ratio less than 1. We discuss afterwards some implications on the disk structure and effects of larger bodies.

Key words: stars: circumstellar matter – stars: individual: HR 4796 A

1. Introduction

HR 4796 A is one of the A type stars showing a high infrared excess ($L_{\text{disk}} / L_{\star} = 5.10^{-3}$) due to the thermal emission from circumstellar dust. The excess is twice that of β Pictoris, the best studied case among Vega-like stars so far. The star age, 8 ± 2 Myr (Stauffer et al., 1995), is about 5 to 15 times less than β Pictoris implying that HR 4796 A is tracing an evolutionary phasis prior to that of β Pictoris.

Koerner et al. (1998) and Jayawardhana et al. (1998) resolved first the circumstellar dust at thermal infrared wavelengths ($\lambda = 10 - 20\ \mu\text{m}$) recently followed by Schneider et al. (1999) in scattered light ($\lambda = 1.1$ and $1.6\ \mu\text{m}$). Interestingly, the disk lies nearly in the direction to HR 4796 B,

a physically bound companion of HR 4796 A (Jura et al., 1993), located $7.7''$ away, *i.e.* 515 AU in projected distance according to the *Hipparcos* star distance $d_{\star} = 67.1_{-3.4}^{+3.5}$ pc.

According to the resolved images, the disk is extending only a few tens of AU outside the peak of the dust distribution assessed to about 70 AU (Schneider et al., 1999). Outer truncation of circumstellar disks within a binary system has been predicted at typical distances of 1/3–1/2 of the binary separation (Papaloizou & Pringle, 1977; Artymowicz & Lubow, 1994). However, the impact of the companion HR 4796 B on the disk extension is still unclear.

In the inner part of the disk, Jura et al. (1995) first suggested a depletion of dust close to the star so as to reproduce the 110 K color temperature deduced from IRAS data. The comparison between resolved mid-IR images and first order modeling (see below) confirmed the necessity of an inner hole in the disk at 55 ± 15 AU from the star for Koerner et al. (1998) and 60 ± 20 AU for Jayawardhana et al. (1998).

According to Koerner et al. (1998), a second population of hotter grains may however lie closer to the star (inside the inner hole). Located at distances similar to those of the zodiacal dust in our Solar System, this dust population would be responsible for both the $12.5\ \mu\text{m}$ detected excess and for a faint emission at $20.8\ \mu\text{m}$ (less than 10% of the total flux at the wavelength) in excess of the resolved disk and centered on the star.

The grains properties are so far poorly constrained. According to Jura et al. (1995), grains smaller than about $3\ \mu\text{m}$ are blown outward by radiation pressure. Considering the Poynting-Robertson effect, they found that the grains are probably larger than $40\ \mu\text{m}$ under the assumption of a 40 AU inner hole. Koerner et al. (1998) used thermal absorption/emission laws for the grains following the model proposed by Backman et al. (1992) for β Pictoris: Q_{abs} is constant for $\lambda < \lambda_0$ and proportional to $(\lambda/\lambda_0)^{-1}$ otherwise, the parameter λ_0 is expected to be related to an effective grain size a_0 in the disk. Although Koerner et al. (1998) constrain λ_0 to $25 \pm 15\ \mu\text{m}$, they do not specify the ratio $\frac{\lambda_0}{a_0}$ in the case of HR 4796 A. This ratio could vary by a factor 40 between the lower and the higher value (Backman et al., 1992).

Before being imaged in the mid-IR spectral range, no optical or near-IR observations successfully resolved the disk around HR 4796 A, if we except for a slight asymmetry in the coronation

Send offprint requests to: J.C. Augereau

^{*} Based on observations collected at the European Southern Observatory, La Silla, Chile

Correspondence to: augereau@obs.ujf-grenoble.fr

graphic adaptive optics system images performed with the ESO adaptive optics system in K' band Mouillet et al. (1997a). Because of the low signal to noise ratio in these data, these results were not presented as a positive detection. Knowing the position angle of the disk, we reduced again these observations and we now marginally detect the disk. After a brief summary of thermal available data, we present in Sect. 2 the newly reduced scattered light images and compare them with more recent and better signal to noise ratio scattered light images (Schneider et al., 1999).

As data become actually more numerous, we wish to better constrain the grain properties in the HR 4796 A disk. Sophisticated grains models developed by Greenberg et al. (1972) succeeded both in reproducing interstellar observations (extinction, polarization (Li & Greenberg, 1997)) and in fitting the shape of the SED of the disk surrounding β Pictoris (Li & Greenberg, 1998; Pantin et al., 1997). In addition, Li & Greenberg (1998) proposed a link between ISM particles and circumstellar evolved environments assuming that dust grains in the β Pictoris disk are of cometary origin (see also Backman & Paresce (1993); Lecavelier des Etangs et al. (1996)) and could be fluffy aggregates of primitive interstellar dust.

In this paper, we adopt a similar approach for the grains in the HR 4796 A disk. We describe in Sect. 3 the disk model assumptions and try to fit (Sects. 4.1 and 4.2) the Spectral Energy Distribution (hereafter SED) to derive some physical and chemical grain properties such as typical size, porosity, presence of ice and finally to estimate if the grains are more similar to interstellar dust grains or to comet-like grains.

In addition, we test whether the presence of a second population responsible for the $10\ \mu\text{m}$ excesses is necessary or not. Given the constraints on the grain distribution derived from the SED fitting, we try to reproduce the thermal and scattered light resolved images (Sect. 4.3). We finally discuss Sect. 5 the implications on the disk dynamics.

2. Available data

2.1. Spectral energy distribution

The available photometric data for the HR 4796 A disk are summarized in Table 1. They include color-corrected IRAS measurements, IRTF bolometer measurements (Fajardo-Acosta et al., 1998), Keck/Mirlin (Koerner et al., 1998) and Cerro Tololo/ OSCIR (Jayawardhana et al., 1998) images and the IRTF bolometer datum obtained by Jura et al. (1993) at $20\ \mu\text{m}$. They also include the available submillimeter data: JCMT upper limit at $800\ \mu\text{m}$ (Jura et al., 1995) and recent SCUBA measurements at $450\ \mu\text{m}$ and $850\ \mu\text{m}$ (Greaves et al., 1999).

2.2. Resolved mid infrared thermal data

Mid-IR images revealed the morphology of the dust distribution sensitive to these wavelengths. Actually, the rather low resolution does not allow to precisely describe the radial shape of the surface brightness along the major axis and its vertical shape.

Table 1. Available infrared and submillimeter measurements. Refer to Sect. 4.1 for the meaning of the mark “*”.

λ [μm]	Excess Φ_{obs} [Jy]	Uncertainty $\Delta\Phi_{\text{obs}}$ [Jy]	Reference
4.80	no excess		Fajardo-A. et al. (1998)
7.80	0.067	0.037	Fajardo-A. et al. (1998)
9.80	no excess		Fajardo-A. et al. (1998)
10.1	0.087	0.026	Fajardo-A. et al. (1998)
10.3	0.057	0.024	Fajardo-A. et al. (1998)
*11.6	0.086	0.070	Fajardo-A. et al. (1998)
*12.0	0.173	0.028	IRAS
*12.5	0.101	0.018	Koerner et al. (1998)
*12.5	0.133	0.027	Fajardo-A. et al. (1998)
*18.2	1.100	0.150	Jayawardhana et al. (1998)
20.0	1.860	unknown	Jura et al. (1993)
*20.8	1.813	0.170	Koerner et al. (1998)
*24.5	2.237	0.700	Koerner et al. (1998)
*25.0	3.250	0.130	IRAS
*60.0	8.630	0.430	IRAS
*100.0	4.300	0.340	IRAS
450.0	0.180	0.150	Greaves et al. (1999)
800.0	<0.028		Jura et al. (1995)
850.0	0.0191	0.0034	Greaves et al. (1999)

However, simple models are consistent with data if the surface density of grains follows a radial power law $r^{-\Gamma}$ where Γ is badly constrained in the range $[0, 2.5]$ (Koerner et al. (1998) and Jayawardhana et al. (1998)). Assuming that the disk is optically and geometrically thin (2-D disk model) and using a Bayesian approach, Koerner et al. (1998) assessed a disk inclination less than about 20° with respect to the line of sight. Indeed, the vertical height to radial height ratio for a given isophote at $20.8\ \mu\text{m}$ is close to 0.35 ± 0.05 which corresponds to a flat disk inclined at $\sin^{-1}(0.35 \pm 0.05) \simeq 20.5 \pm 3^\circ$ from edge-on. Finally, both Koerner et al. (1998) and Jayawardhana et al. (1998) images are consistent with a disk located at the position angle (PA) in the ranges: $[22^\circ, 34^\circ]$ for Koerner et al. (1998) and $[20^\circ, 40^\circ]$ for Jayawardhana et al. (1998).

2.3. Resolved near infrared data

2.3.1. Reduction procedure

The coronagraphic observations we reinvestigate in this paper have been first presented in Mouillet et al. (1997a). This paper also describes the reduction procedure used. A main step in coronagraphic data reduction is the removal of the scattered light remaining around the mask. This implies to use a comparison star whose scattered light is scaled to that of the object of interest. The scaling factor is generally estimated by azimuthally averaging the division of the star of interest by the comparison star. Azimuthal averaging over 360° prevents from detecting pole on disks and decreases the chance of detection of inclined disks or faint structures. Knowing the orientation of the disk, we were able to estimate more precisely the scaling factor in a section perpendicular to the disk.

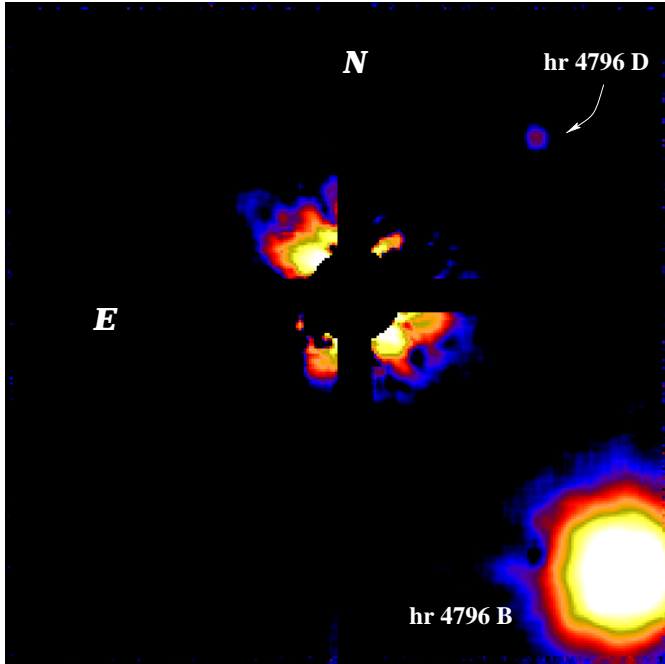


Fig. 1. Newly reduced coronagraphic image in logarithmic scale of HR 4796 A in K' filter revealing an excess close to the expected PA. The field-of-view is $13'' \times 13''$ with a sampling of $0.05''$ per pixel, smoothed to $0.2''$. The numerical mask occults up to about 60 AU ($0.9''$) in radius. One can note the faint companion HR 4796 D ($K' = 14.5$) at $PA = 311^\circ$ detected by Kalas & Jewitt (1993) and Mouillet et al. (1997a).

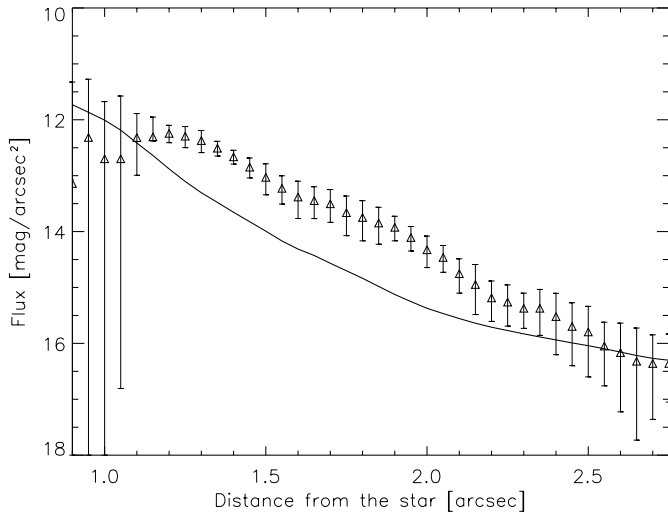


Fig. 2. NE residual signal in the region around $PA = 30^\circ$ compared to the noise (plain line). The latter is interpreted as the detection limit of the disk. The residual signal in the regions perpendicular to the disk is close to 0 on average (not represented in this logarithmic scale). On the contrary, the residual signal in the NE region is continuously greater than the noise between $1.1'' - 1.2''$ and $2.3'' - 2.4''$.

2.3.2. Radial excess almost in the direction of HR 4796 B

We present in Fig. 1 the newly reduced coronagraphic image of HR 4796 A in K' band. An excess is present in the NE and SW regions. Due to the spreading of the excess and due to the rather

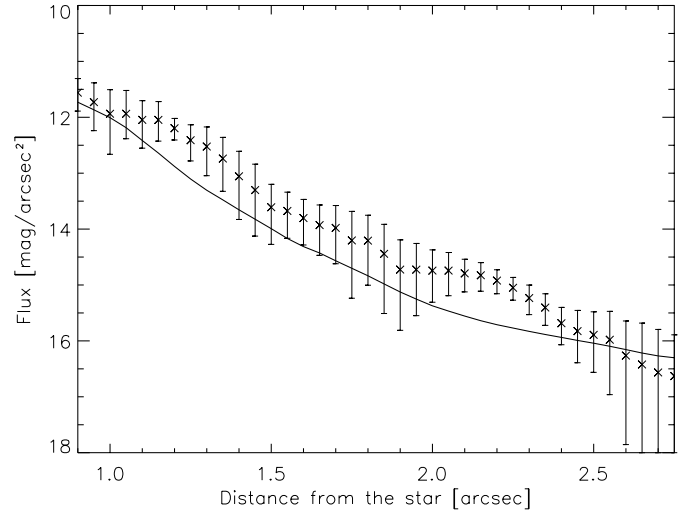


Fig. 3. Same as Fig. 2 but for the SW region (around $PA = 210^\circ$).

low signal to noise, the position angle is badly constrained but is roughly consistent with both the PA deduced from previous images and the direction of the physical companion HR 4796 B. We extract the residual signal azimuthally averaged in the ranges of PA : $[20^\circ, 40^\circ]$ and $[200^\circ, 220^\circ]$ as a function of the distance from the star. We plot in Figs. 2 and 3 the comparison with the noise on the image estimated in the regions perpendicular to the excess. Between about $1.1''$ and $2.3''$, the NE and SW remaining signals appear above the noise whereas in the perpendicular region the residual signal fluctuates around 0 which characterizes the lack of circumstellar structure in the NW and SE regions. Although the signal to noise ratio is rather low close to the star, we find an azimuthally averaged surface brightness at $1.1'' - 1.2''$ ($75 - 80$ AU) from the star: 12.2 ± 0.5 mag.arcsec $^{-2}$ quite similar to the range $11.7 - 12.7$ mag.arcsec $^{-2}$ measured in H band by Schneider et al. (1999) between $1.1''$ and $1.2''$. The observed surface brightness is roughly proportional to r^{-5} but deconvolved images would lead to steeper slopes as also suggested by Schneider et al. (1999) observations.

3. Disk model assumptions

3.1. Grain distribution

We adopt a parametrical approach to describe the grain distribution in the disk similarly to that adopted to describe the β Pictoris disk (Artymowicz et al., 1989):

$$n(r, z) = n_0 R(r) Z(r, z)$$

where $n(r, z)$ is axisymmetrical grain density, $R(r)$ and $Z(r, z)$ are respectively the radial and the vertical no-dimensional distributions and n_0 the grain density at the normalized distance $r = r_0$ when $z = 0$. The distance r_0 is fixed to 70 AU in all the simulations and $R(r)$ is normalized so as to have $R(r_0) = 1$.

Following Artymowicz et al. (1989), we assume a vertical distribution characterized by an exponential with a shape de-

pending on the parameter γ ($\gamma > 0$):

$$Z(r, z) = \exp\left(-\left(\frac{|z|}{\zeta(r)}\right)^\gamma\right) \text{ with } \zeta(r) = \zeta_{r_0} \left(\frac{r}{r_0}\right)^\beta$$

where the radial shape of the vertical scale height $\zeta(r)$ depends on the parameter $\beta > 0$. ζ_{r_0} is the normalized height when $r = r_0$. This notation is useful because the integration of $Z(r, z)$ along the vertical axis (z) of the disk is proportional to r^β . Therefore, the surface density of the grains, which is the interesting quantity to model the photometric data, can be written as:

$$\sigma(r) = \int_{-\infty}^{+\infty} n(r, z) dz = \sigma_0 \times R(r) \left(\frac{r}{r_0}\right)^\beta$$

where $\sigma_0 = C_\gamma n_0 \zeta_{r_0}$ and $C_\gamma = 2 \int_0^{+\infty} \exp(-x^\gamma) dx$ (x is a non-dimensional variable).

We parametrize the radial distribution of the grains with a smooth combination of two power laws:

$$R(r) \propto \left\{ \left(\frac{r}{r_c}\right)^{-2\alpha_{\text{in}}} + \left(\frac{r}{r_c}\right)^{-2\alpha_{\text{out}}} \right\}^{-\frac{1}{2}}$$

with $\alpha_{\text{in}} > 0$ and $\alpha_{\text{out}} < 0$. The inner disk is assumed to be cut-off at the distance corresponding to the grain sublimation temperature (~ 1800 K). The maximum of the surface density $\sigma(r)$ is not r_c but also depends on α_{in} , α_{out} and β :

$$r_{\text{max}(\sigma)} = \left(\frac{\Gamma_{\text{in}}}{-\Gamma_{\text{out}}}\right)^{(2\Gamma_{\text{in}} - 2\Gamma_{\text{out}})^{-1}} r_c \quad (1)$$

with $\Gamma_{\text{in}} = \alpha_{\text{in}} + \beta$ and $\Gamma_{\text{out}} = \alpha_{\text{out}} + \beta$. Outside this maximum, $\sigma(r)$ is roughly proportional to $r^{\Gamma_{\text{out}}}$, and roughly proportional to $r^{\Gamma_{\text{in}}}$ inside. Finally, the SED computation requires a four parameters grain distribution: r_c , Γ_{in} , Γ_{out} , and σ_0 .

3.2. Grains characteristics

3.2.1. Composition assumptions

We assume that the grains are porous aggregates made of a silicate core coated by an organic refractory mantle (Greenberg (1986) and references therein, Pollack et al. (1994)). Vacuum is assumed to fill the holes due to porosity. If the grain temperature is less than the sublimation temperature of the H₂O ice ($T_{\text{sub}, \text{H}_2\text{O}} \simeq 110 - 120$ K), the H₂O ice is able to fill all or part of the vacuum in the grain. The relative abundances of each compound are given by the volume ratios: $q_{\text{SiOr}} = \frac{V_{\text{Si}}}{V_{\text{Or}}}$ and $q_{\text{SiOrH}_2\text{O}} = \frac{V_{\text{Si}} + V_{\text{Or}}}{V_{\text{H}_2\text{O}}}$, where V_{Si} , V_{Or} and $V_{\text{H}_2\text{O}}$ are respectively the silicate, the organic refractories and the H₂O volumes. The corresponding grain density ρ_g is:

$$\rho_g = (1 - P) * \left(\frac{q_{\text{SiOr}} \rho_{\text{Si}}}{1 + q_{\text{SiOr}}} + \frac{\rho_{\text{Or}}}{1 + q_{\text{SiOr}}} + \frac{\rho_{\text{H}_2\text{O}}}{q_{\text{SiOrH}_2\text{O}}} \right) \quad (2)$$

where the individual densities are: $\rho_{\text{Si}} = 3.5 \text{ g.cm}^{-3}$, $\rho_{\text{Or}} = 1.8 \text{ g.cm}^{-3}$ and $\rho_{\text{H}_2\text{O}} = 1.2 \text{ g.cm}^{-3}$. Given the Si+or aggregate

porosity P , the corresponding percentage of vacuum removed due to the presence of the H₂O ice is therefore:

$$p_{\text{H}_2\text{O}} = \left(\frac{1}{P} - 1\right) \frac{100}{q_{\text{SiOrH}_2\text{O}}} \% .$$

Li & Greenberg (1998) proposed two extreme types of dust in Vega-like disks: amorphous or crystalline grains mainly depending on the evolution of the circumstellar environment and probably depending on the spectral type. In this paper, we investigate the two following types of grains:

1. “ISM-like grains”:
 - amorphous Si and amorphous H₂O ice,
 - $q_{\text{SiOr}} \simeq \frac{1}{2.12}$ for spherical grains and $q_{\text{SiOr}} \simeq \frac{1}{2.94}$ for cylindrical grains (Li & Greenberg, 1997),
 - porosity P between 0.45 (Mathis, 1996) and 0.8 (Mathis & Whiffen, 1989).
2. “comet-like grains”:
 - crystalline Si and crystalline H₂O ice,
 - $q_{\text{SiOr}} \simeq \frac{1}{2}$ (comet Halley, Greenberg (1998)),
 - porosity P between 0.93 and 0.975 (comet Halley, Greenberg & Hage (1990)).

For all the models, we consider spherical grains and therefore we fixed the volume ratio q_{SiOr} to $\frac{1}{2}$.

3.2.2. Optical properties computation

We compute theoretical absorption/emission and scattering efficiencies for spherical grains via Mie theory (Bohren & Huffman, 1983) knowing the ratio $x = \frac{a}{\lambda}$ where a is the grain radius and knowing $m(\lambda)$ the complex index of refraction of the grain. In some extreme cases, Mie theory is not efficient: we used the Rayleigh-Gans theory when $|m(\lambda)|x > 1000$ and $|m(\lambda) - 1|x < 0.001$ or the geometric optics when $|m(\lambda)|x > 1000$ and $|m(\lambda) - 1|x > 0.001$ (Laor & Draine, 1993).

We adopt the Maxwell-Garnett effective medium (MGEM) theory to compute $m(\lambda)$ for the mixture (Si + “or” + H₂O ice and/or vacuum) given the complex indexes of refraction of each compound, the volumes ratios and the porosity. We prefer the MGEM theory to the Bruggman effective medium (BEM) theory because the MGEM theory considers that a mixture is composed of an inclusion (the core) embedded in a homogeneous matrix (the mantle) whereas the BEM theory treats both components in the same way (Bohren & Huffman, 1983).

3.2.3. Optical constants

The wavelength dependence of the grain complex index of refraction $m(\lambda)$ depends on the individual compounds:

→ *Silicates*: there is presently no consensus on what could be “representative” astronomical silicates. In the case of amorphous silicates, we arbitrarily adopt the modified (Laor & Draine, 1993) Draine & Lee optical constants

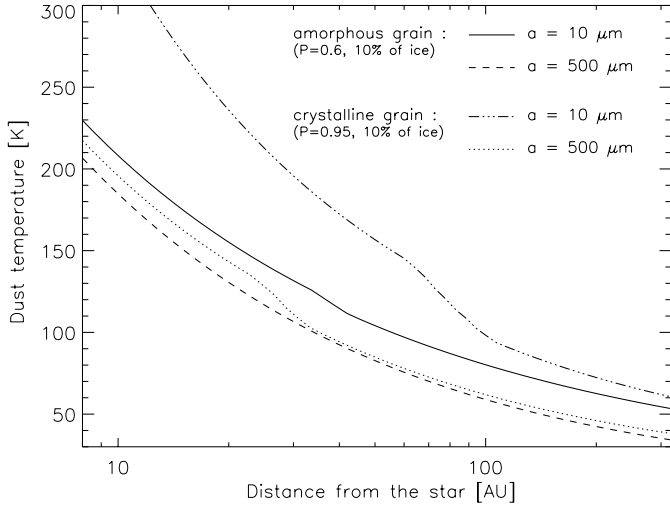


Fig. 4. Grain temperature versus the distance from the star for amorphous and crystalline grains and for different grain sizes a . The grain temperature has been computed from the energetic balance between the absorbed flux and the emitted flux over all the spectrum. We use a Kurucz spectrum for an A1V star scaled to the V magnitude and extrapolated with a λ^{-4} power law (Rayleigh-Jeans) to simulate the star flux. The break in the grain temperature is due to H_2O ice sublimation (see also Fig. 5). The dust temperature of the icy grains follows a radial power law r^q with q between -0.36 and -0.47 for the amorphous grains and q between -0.40 and -0.43 for the crystalline grains.

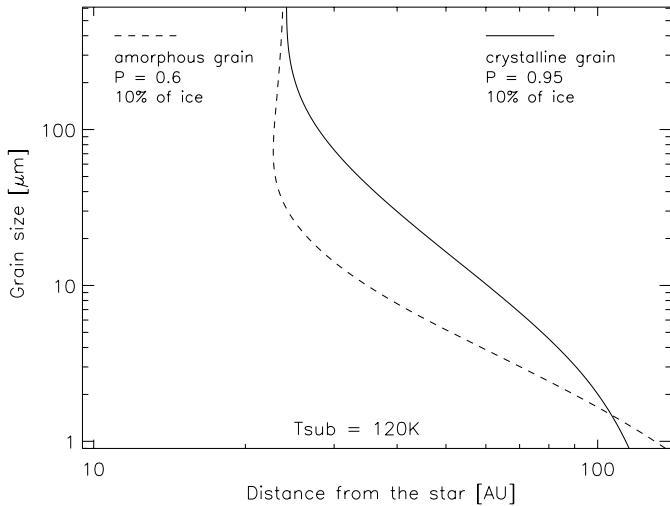


Fig. 5. Grain size corresponding to the H_2O ice sublimation limit versus the distance from the star for a typical amorphous grain and a typical crystalline grain. On the left side of the curve, the ice is sublimated; on the right, grains are icy.

(Draine & Lee, 1984; Draine, 1985). In the case of crystalline silicates, we adopt the analytic complex indexes of refraction for crystalline olivine particles proposed by Mukai & Koike (1990) between $\lambda = 7 \mu\text{m}$ and $\lambda = 200 \mu\text{m}$ and we extrapolate (as Li & Greenberg (1998)) with Draine & Lee (1984) optical constants for $\lambda < 7 \mu\text{m}$ and $\lambda > 200 \mu\text{m}$.

→ *Organic refractories*: we adopt the optical constants computed by Li & Greenberg (1997) (a full discussion on organic refractories can be found in this paper).

→ *H_2O ice*: in the case of amorphous ice and between $\lambda = 1.3 \mu\text{m}$ and $\lambda = 144 \mu\text{m}$, we use the optical constants derived from Fink & Sill (1982) ($T = 82 \text{ K}$) combined with the 100 K data from Hudgins et al. (1993). In the case of crystalline ice and between $\lambda = 0.89 \mu\text{m}$ and $\lambda = 333 \mu\text{m}$, we adopt the hexagonal water ice optical constants at a temperature of about 100 K derived by Ockman (1958) and Bertie et al. (1969). For both the amorphous and crystalline ices, we extrapolate with the Warren (1984) optical constants.

3.2.4. Grain size distribution

The choice of the grain size distribution $n(a)$ in the disk is a key step in the grain modeling. We assume either a single grain size ($a = a_0$) or a grain size distribution following the classical power law $n(a)da \propto a^{-\kappa}da$ in the range $[a_{\min}, a_{\max}]$ which may be better suited if the grains result from collisions among larger bodies. We fixed $\kappa = 3.5$, a typical value usually assumed for collisional disks (Hellyer, 1970; Mathis et al., 1977). We use: $n(a)da = 2.5 x^{-3.5} dx$ with $x = a/a_{\min}$ so as to have:

$$\int_1^{x_{\max}} 2.5 x^{-3.5} dx = 1 \quad \text{with} \quad x_{\max} = \frac{a_{\max}}{a_{\min}} \gg 1$$

Finally, the grains are characterized by their amorphous or crystalline nature and by the three free parameters: a_0 , P and $p_{\text{H}_2\text{O}}$ for a single grain size distribution or by the four free parameters: a_{\min} , a_{\max} , P and $p_{\text{H}_2\text{O}}$ for a -3.5 power law grain size distribution. Some examples of the dust temperature and of the grain size corresponding to the H_2O ice sublimation limit versus the distance from the star are plotted Figs. 4 and 5 respectively.

4. Modelling

4.1. SED fitting assuming a single grain size distribution

Our aim is to derive the dust distribution and to constrain the grains properties with the available measurements.

We already have a constraint on the peak of the grain distribution (r_c). Indeed, the shape of the isophotes in scattered light at $\lambda = 1.1 \mu\text{m}$ and $\lambda = 1.6 \mu\text{m}$ (Schneider et al., 1999) suggests faint anisotropic scattering properties for the grains at these wavelengths (see also 4.3.2) implying that the observed maximum surface brightness at roughly 70 AU is probably close to the peak of the grain distribution. We therefore fix $r_c = 70 \text{ AU}$.

We let the 6 remaining parameters free in their respective ranges:

- the 2 grains distribution parameters: Γ_{in} and Γ_{out} in $[2, 13]$ and $[-13, -2]$ respectively,
- the 3 grains characteristics parameters: grain size a_0 in $[1 \mu\text{m}, 600 \mu\text{m}]$, porosity P in the range $[0.45, 0.8]$ if the

Table 2. Sets of parameters providing the best fits of the 10–100 μm SED assuming a single grain size distribution and amorphous grains (models **#1**, **#2** and **#3**) or crystalline grains (models **#4**, **#5** and **#6**). We also add some interesting quantities such as: the effective grain size $a_0^{\text{eff}} = a(1 - P)^{1/3}$ which represents the size of a not porous grain with the same mass as the grain with the size a_0 and the porosity P , the final grain porosity $P_{\text{withH}_2\text{O}} = P(1 - p_{\text{H}_2\text{O}}/100)$ taking into account that $p_{\text{H}_2\text{O}}$ % of the vacuum has been removed and filled with H_2O ice, the grain density ρ_g (Eq. 2) and the disk mass $M_d(a_0)$. For all the models, the peak of the surface density is close to $r_{\text{max}(\sigma)} = 67$ AU.

n°	Γ_{in}	Γ_{out}	σ_0 [grains.cm ⁻²]	a_0 [μm]	P	$p_{\text{H}_2\text{O}}$	χ^2	a_0^{eff} [μm]	$P_{\text{withH}_2\text{O}}$	ρ_g [g.cm ⁻³]	$M_d(a_0)$ [10 ⁻² M_\oplus]
<i>amorphous</i>											
#1	2.94	-12.52	0.95	440	0.79	0.9	11.2	262	0.78	0.51	7.84
#2	2.83	-12.21	5.45	183	0.65	0.5	11.6	130	0.64	0.84	5.50
#3	2.91	-11.97	3.17	242	0.72	2.3	11.9	158	0.70	0.68	5.85
<i>crystalline</i>											
#4	2.88	-10.49	8.11	147	0.93	38	5.7	59	0.58	0.59	3.04
#5	3.11	-7.27	1.06	391	0.975	19	6.7	114	0.79	0.28	4.21
#6	3.30	-11.85	0.74	505	0.975	15	7.5	148	0.83	0.23	4.09

grains are amorphous or in [0.93, 0.975] if the grains are crystalline and percentage of H_2O ice $p_{\text{H}_2\text{O}}$ in [0 %, 50 %].

- the normalized dust surface density σ_0 : given a set of the 5 previous parameters, the normalized dust surface density σ_0 is used as a flux scaling factor so as to provide the best fit of the SED.

As a first step, we try to fit the 10–100 μm SED only. Our aim is to minimize the χ^2 :

$$\chi^2 = \sum_{i=1}^N \left(\frac{\Phi_{\text{obs}}(\lambda_i) - \Phi_{\text{sim}}(\lambda_i)}{\Delta\Phi_{\text{obs}}(\lambda_i)} \right)^2$$

where $\Phi_{\text{sim}}(\lambda_i)$ are the simulated flux and N the number of data and discuss afterwards the consistency with thermal and scattered light resolved images.

We start the minimization with a random vector of the parameters. One has to note that we limit N to the ten data marked with a “*”. Indeed, taking into account the numerous measurements at about 10 μm , compared to the few data at larger wavelengths, would give a too high weight to this SED region. The χ^2 probability $\wp(\chi^2, N - 6)$ gives us a criterion for the quality of the fit. For example, so as to have $\wp > 10\%$ we need $\chi^2 < 7.78$ with $N = 10$.

We present Table 2 six different sets of the parameters which lead to the best 10–100 μm SED fitting assuming a single grain size distribution a_0 and a single grain distribution.

The 3 crystalline grains models satisfy the χ^2 criterion: $\wp > 10\%$ whereas the amorphous grains models do not. Amorphous grains do not provide a proper fit of the 10–12.5 μm data. The crystalline hypothesis reproduce very well the 10 μm emission feature. Furthermore, the 10.1 μm and 10.3 μm data, not used to derive the parameters, are also well fitted with the model (Fig. 6). Note that the 20 μm –100 μm continuum is fitted both with crystalline grains and with amorphous grains.

Grains with $a_0^{\text{eff}} > 60$ μm are needed to reproduce the shape of the SED (see Table 2 for the definition of a_0^{eff}) which leads to grains sizes a_0 larger than 150 μm . Most of the grains are located further than the H_2O ice sublimation distance (Fig. 5)

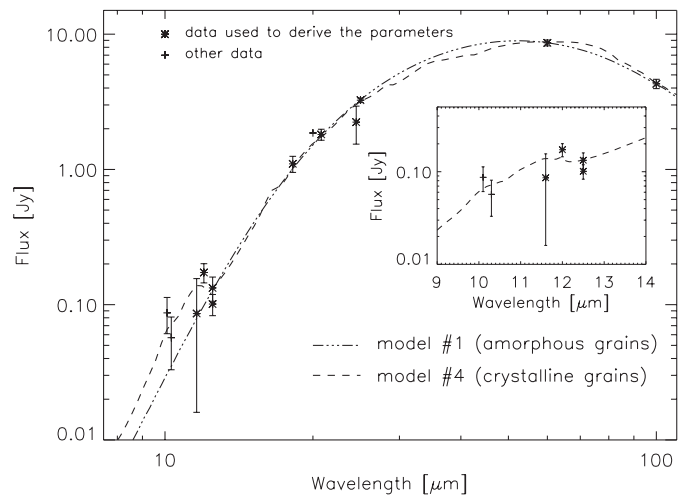


Fig. 6. Two fits of the 10 μm –100 μm Spectral Energy Distribution of the HR 4796 A disk assuming a single grain size distribution $a = a_0$ and a single grain distribution peaked at $r_c = 70$ AU from the star (parameters from Table 2).

and have to be significantly icy: $p_{\text{H}_2\text{O}} > 15 - 20\%$ (consistent with Jura et al. (1998) assumptions).

We find Γ_{in} to be close to 3 and the outer surface density (Γ_{out}) to be steeper than r^{-7} (more probably as steep as r^{-10}). Whereas the outer slope of the grain surface density is consistent with the scattered light images, the inner slope is not. It would induce much more light in the inner disk than observed. Indeed, an r^3 inner surface density yields an inner midplane surface brightness in scattered light less steep than at least $r^{2-\beta}$ (case of an edge-on disk assuming isotropic scattering properties for the grains, Nakano (1990)). As an example, we plot Fig. 7 the surface brightness contours for a 15° tilted (from edge-on) disk in scattered light at $\lambda = 1.1$ μm .

Taking into account the constraint from scattered light images, we therefore try to derive the grains properties which could reproduce the 10–100 μm SED with $\Gamma_{\text{in}} \simeq 10$. Such an inner slope acts as a cut-off for the short wavelengths efficient emit-

Table 3. Sets of parameters providing the best fits of the full SED assuming a collisional grain size distribution ($\propto a^{-3.5}$) and amorphous grains (models #7, #8 and #9) or crystalline grains (models #10, #11 and #12). Refer to Table 2 for the definition of the quantities a^{eff} , $P_{\text{withH}_2\text{O}}$ and ρ_g . $M_d(a_{\text{min}})$ is the mass corresponding to the smallest grains and $M_d = 2M_d(a_{\text{min}})\sqrt{a_{\text{max}}/a_{\text{min}}}$ is the total disk mass. The peak of the surface density $r_{\text{max}(\sigma)}$ is close to r_c .

n°	σ_0 [grains.cm $^{-2}$]	a_{min} [μm]	a_{max} [cm]	P	$p_{\text{H}_2\text{O}}$	χ^2	$a_{\text{min}}^{\text{eff}}$ [μm]	$a_{\text{max}}^{\text{eff}}$ [cm]	$P_{\text{withH}_2\text{O}}$	ρ_g [g.cm $^{-3}$]	$M_d(a_{\text{min}})$ [$10^{-3} M_\oplus$]	M_d [M_\oplus]
<i>amorphous</i>												
#7	1.08×10^4	4	18	0.57	39	18	3	14	0.35	1.29	3.78	1.59
#8	8.10×10^3	5	410	0.63	35	18	3	294	0.41	1.14	2.81	5.25
#9	1.69×10^3	10	137	0.8	12	27	6	80	0.70	0.59	3.15	2.31
<i>crystalline</i>												
#10	1.02×10^3	12	246	0.93	18	54	5	101	0.77	0.36	1.98	1.78
#11	1.27×10^2	35	296	0.975	7	55	10	87	0.88	0.14	2.28	1.33
#12	4.11×10^1	64	116	0.975	4	84	18	34	0.94	0.10	3.15	0.85

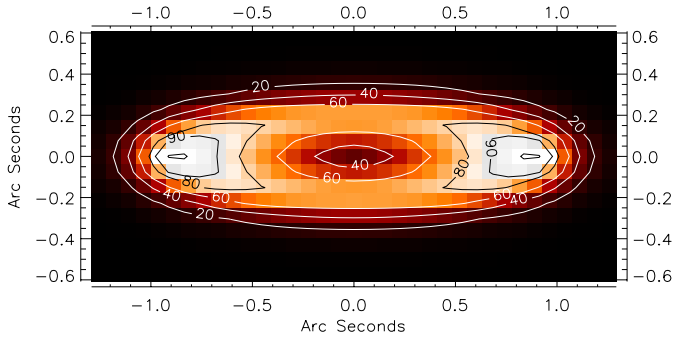


Fig. 7. Surface brightness contours of a 15° tilted disk in scattered light ($\lambda = 1.1 \mu\text{m}$) assuming the set of parameters #4 (Table 2) and isotropic scattering properties for the grains. We also assume a flat disk: $\beta = 0.75$, $\zeta_{r_0} = 4\text{AU}$ and an exponential vertical distribution: $\gamma = 1$. The contour levels are in an arbitrary unit; the upper level is fixed to 100. In the inner part of the disk, the surface brightness decreases slowly with the distance from the star: for instance, the surface brightness at $0.5''$ from the distance corresponding to the upper level still represents 60% of the maximum surface brightness. Such an inner dust distribution ($\Gamma_{\text{in}} \simeq 3$) is then not consistent with HST observations (Schneider et al., 1999).

ters which are located close to the star. Under these assumptions neither the crystalline nor the amorphous grains provide good fits of the 10–100 μm SED (Fig. 8). In the present case, we also exclude to add an inner dust distribution (typically inside 50 AU) to fit the SED at short wavelengths. In this scheme, the inner and outer disks would have similar contributions (flux) at 20 μm (Fig. 8), which is not compatible with 20 μm resolved images (Koerner et al., 1998; Jayawardhana et al., 1998).

In conclusion, assuming a single grain size distribution, we are able to properly fit the 10–100 μm SED but not the resolved images. Moreover, the presence of hot crystalline grains seems necessary to fit the 10 μm measurements.

4.2. SED fitting assuming a grain size distribution proportional to $a^{-3.5}$

We now assume a collisional grain size distribution $n(a)$ proportional to $a^{-3.5}$ between a minimum and a maximum grain

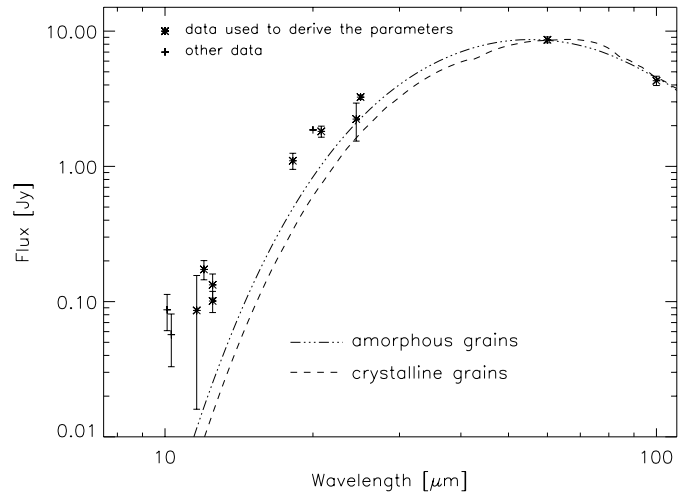


Fig. 8. Same as Fig. 6 but assuming $\Gamma_{\text{in}} = 10$.

size a_{min} and a_{max} . We also assume that the relative abundances of the different compounds and the porosity do not depend on the grain size.

We adopt a spatial grain distribution consistent with the scattered light images and therefore fix r_c to 70 AU, the inner slope Γ_{in} to 10 and the outer slope Γ_{out} to -11.5 . The grain properties are now the free parameters left.

4.2.1. Single grain population

We try to fit the SED by minimizing the χ^2 associated to the 10 data marked with a “*” in Table 1 plus the 850 μm measurement. We keep the porosity P and the percentage of H_2O ice free in the same ranges as for the single grain size distribution and investigate the respective broad ranges [1 μm , 500 μm] and [600 μm , 5 m] for the minimum a_{min} and the maximum a_{max} grain sizes.

The results are summarized in Table 3. Whatever the nature of the grains, the fits do not satisfy the χ^2 criterion ($\varphi > 10\%$ if $\chi^2 < 9.24$), but micronic to centimetric amorphous grains better reproduce the shape of the SED continuum than crystalline grains (Fig. 9). Therefore, crystalline grains (if any) probably

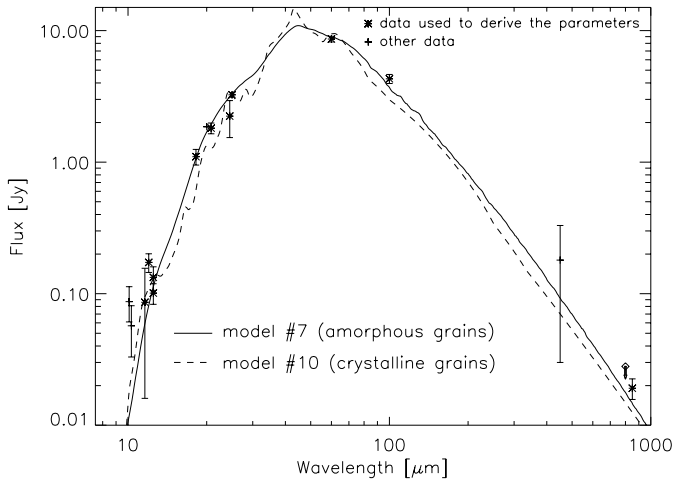


Fig. 9. Two fits of the full SED assuming a collisional grain size distribution and a single dust population peaked at 70 AU from the star. The 10 μm and 850 μm data are not properly fitted.

represent a minor part of the grain population in the annulus peaked at 70 AU. On the other hand, the 10 μm measurements are not well reproduced with the amorphous grain model still suggesting (see previous section) the presence of a small amount of crystalline grains in order to significantly emit at 10 μm but not at larger wavelengths. If there are crystalline grains at 70 AU, they are neither numerous nor hot enough to produce such a spectral energy distribution. Therefore, if the 10 μm data are not overestimated (especially the 10.1 μm , the 10.3 μm and the 12 μm measurements), we can exclude to fit the full SED from the NIR to the submillimeter wavelengths with the same dust population.

4.2.2. Two grain populations

→ *The cold annulus:* We now assume that the excesses at large wavelengths mainly come from the annulus resolved in scattered light. This is consistent in terms of spatial extension with the disk observed at 20.8 μm (Koerner et al., 1998) suggesting that the same dust population may be responsible for both the 20.8 μm and the 1.1 μm images.

We therefore try to fit the 5 data at wavelengths larger than 20 μm (excluding the 24.5 μm and 450 μm data due to too high uncertainties) and try to constrain the grains properties consistent with the colder part of the SED. We fix the porosity P to 0.6 for amorphous grains or to 0.93 for crystalline grains as suggested by the full SED fitting (Table 3). We keep the three parameters a_{\min} , a_{\max} and $p_{\text{H}_2\text{O}}$ free in the same ranges as in the previous Sect. (4.2.1).

The results of the χ^2 minimization are summarized in Table 4 and Fig. 10 shows the best fits for each grain nature. The cold SED continuum is remarkably well fitted ($\varphi > 10\%$ if $\chi^2 < 2.71$) with amorphous grains whereas the crystalline grains lead to very poor χ^2 . Very little icy grains ($p_{\text{H}_2\text{O}} < 5\%$) with sizes larger than 10 μm (15 μm if we assume $P = 0.7$) are required to fit the 20–25 μm data and bodies as large as a few

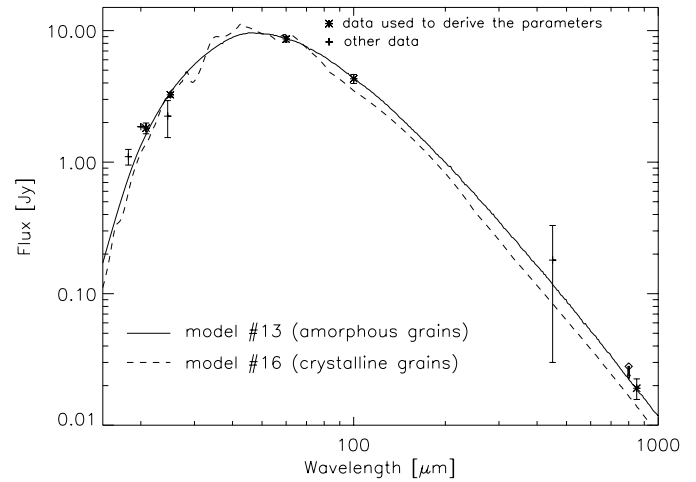


Fig. 10. Two fits of the 20–850 μm SED assuming the dust resolved in scattered light and peaked at 70 AU from the star is responsible for the excesses at wavelengths larger than about 20 μm .

meters are necessary to correctly reproduce the submillimeter excess. This leads to an outer disk mass larger than a few Earth masses.

→ *The hot dust population:* At 20.8 μm , the simulated cold annulus (model #13) contributes to about 90% of the measured excess at this wavelength. Therefore and conversely to the single grain size model, the addition of a second grain population would not modify the consistency between the simulated thermal images at 20.8 μm and the observations.

We therefore subtract the simulated flux coming from the outer annulus (model #13) to the observed excesses and try to fit the remaining excesses with a second dust distribution made of crystalline grains (suggested by the single grain size distribution fitting (Sect. 4.1)). The full SED assuming two grain populations is now very well fitted (see Fig. 11). In this example, the inner dust distribution represents a mass of about $3.5 \times 10^{-5} M_{\oplus}$ made of 450 μm crystalline grains ($P = 0.97$) peaked at 9 AU from the star and heated at about 210–220 K (see for example Fig. 4).

4.3. Images

We now adopt the two grain populations model from previous Sect. (4.2.2): an amorphous dust population peaked at 70 AU (model #13) plus a crystalline dust population at 9 AU from the star. We assume a disk inclination i_{tilt} of 15° with respect to the line of sight.

4.3.1. Thermal images

We simulate the disk in thermal emission so as to derive further informations on the vertical shape of the disk (parameters ζ_{r_0} , γ and β assumed to be constant over all the disk). We actually have very few constraints on the vertical shape of the disk, also we arbitrarily start with parameters derived for β Pictoris disk:

Table 4. Sets of parameters providing the best fits of the 20–850 μm SED assuming a collisionnal grain size distribution ($\propto a^{-3.5}$) and amorphous grains (models #13, #14 and #15) or crystalline grains (models #16, #17 and #18). Refer to Table 3 for the definition of the quantities a^{eff} , $P_{\text{withH}_2\text{O}}$, ρ_g , $M_d(a_{\text{min}})$ and M_d . The peak of the surface density $r_{\text{max}(\sigma)}$ is close to r_c .

n°	σ_0 [grains.cm $^{-2}$]	a_{min} [μm]	a_{max} [cm]	$p_{\text{H}_2\text{O}}$	χ^2	$a_{\text{min}}^{\text{eff}}$ [μm]	$a_{\text{max}}^{\text{eff}}$ [cm]	$P_{\text{withH}_2\text{O}}$	ρ_g [g.cm $^{-3}$]	$M_d(a_{\text{min}})$ [$10^{-3} M_\oplus$]	M_d [M_\oplus]
<i>amorphous</i>											
#13	1.79×10^3	10	143	3.03	1.38	7	106	0.58	0.97	5.10	3.87
#14	1.65×10^3	10	291	2.12	2.06	7	214	0.59	0.96	5.10	5.43
#15	1.38×10^3	11	36	0.13	2.72	8	27	0.60	0.95	5.58	2.01
<i>crystalline</i>											
#16	2.70×10^1	80	208	2.95	17.3	33	86	0.90	0.20	8.00	2.58
#17	1.12×10^2	38	359	6.54	22.8	16	148	0.87	0.24	4.53	2.76
#18	9.94×10^1	41	276	6.49	23.5	17	114	0.87	0.24	4.80	2.50

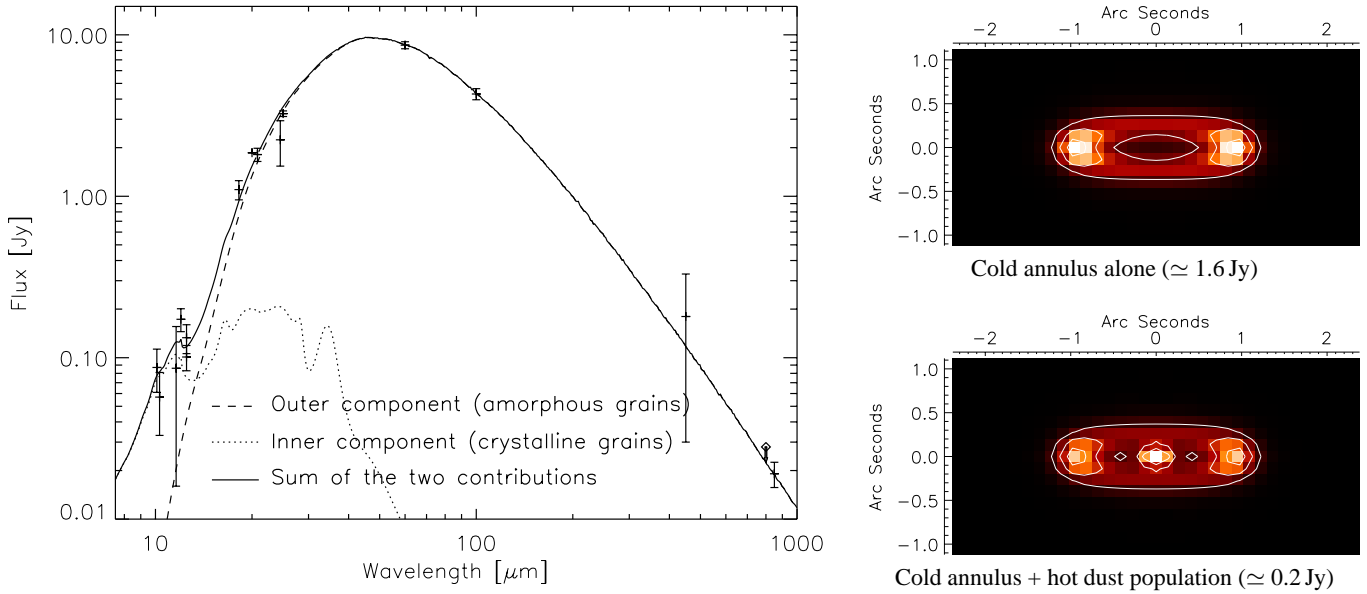


Fig. 11. *Left:* the full SED fitting assuming two dust populations: model #13 + an inner dust population (see text). *Right:* simulated disks in thermal emission at $\lambda = 20.8 \mu\text{m}$ assuming grain properties and surface density derived from the SED fitting. We also assume a vertical structure quite similar to the β Pictoris disk one. We simulate the disks with the same pixel size ($0.14''$) as the observations performed by Koerner et al. (1998). The images have been convolved with an Airy pattern to take into account the PSF of a 10 m telescope at $\lambda = 20.8 \mu\text{m}$.

opening angle of the disk $\sim 6^\circ$ (i.e. $\zeta_{r_0} \sim 4 \text{ AU}$), $\beta \sim 0.75$ and $\gamma \sim 1$ (Mouillet et al., 1997a). We plot (Fig. 11) the simulated disk at $\lambda = 20.8 \mu\text{m}$. The simulated vertical height to radial height ratios for a given isophote are between 0.32 and 0.35; they compare very well with the values 0.35 ± 0.5 from Koerner et al. (1998).

If we afterwards simulate the thermal images for different sets of the parameters ζ_{r_0} , β and γ , we get a few interesting results:

- The normalized height ζ_{r_0} at $r_0 = 70 \text{ AU}$ is probably less than about 7–8 AU leading to opening angles of the disk smaller than about 15° . For example, $\zeta_{r_0} = 10 \text{ AU}$ provides a too large vertical structure and the vertical spreading of the dust yields a smaller surface flux density for the outer annulus compared to the inner one. Such a high contrast is not observed.

- The parameter β is badly constrained: 0.75 provides a good shape of the isophotes (Fig. 11) but 1.5 might also be a correct value.
- Given the resolution of the observations, the parameter γ is completely undetermined.

4.3.2. Scattered light images

To simulate the scattered light images, we adopt the empirical Henyey-Greenstein phase function (Henyey & Greenstein, 1941) which depends on the single parameter $|g|$ (0 for isotropic scattering and 1 for total forward or backward scattering). Indeed, theoretical phase functions from Mie theory are probably not realistic for porous fluffy grains.

We simulate at $\lambda = 1.1 \mu\text{m}$ the *cold annulus*, which is responsible for the scattered light images, assuming different

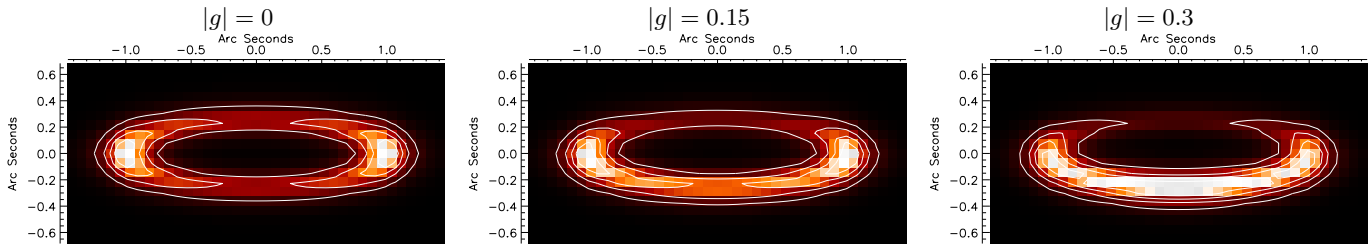


Fig. 12. Simulations of the cold annulus peaked at 70 AU in scattered light at $\lambda = 1.1 \mu\text{m}$ for different asymmetry factors $|g|$; the inner hot dust not observable has not been added. We assume the same spatial distribution and grains properties parameters as Fig. 11. The pixel size is $0.076''$ (Schneider et al., 1999).

values of the parameter $|g|$. As anticipated, due to the disk inclination with respect to the line of sight, the morphology of the observed disk strongly depends on the anisotropic scattering properties (Fig. 12). The observed isophotes at $\lambda = 1.1 \mu\text{m}$ (Schneider et al., 1999) implies that the asymmetry factor $|g|$ is smaller than 0.15.

At $1.1 \mu\text{m}$, the simulated cold annulus scattered a total flux close to 8.6 mJy (5.0 mJy at $1.6 \mu\text{m}$) assuming $|g| \simeq 0$. The integrated flux density corresponding to the detected part of the annulus with HST (outside $0.65''$ in radius) represents 5.2 mJy at $\lambda = 1.1 \mu\text{m}$, *i.e.* only slightly smaller than 7.5 ± 0.5 mJy from Schneider et al. (1999).

We also simulate the disk in K' band. At $1.1''$ from the star along the major axis of the annulus, the flux density is about $16 \mu\text{Jy}$ in a $0.05'' \times 0.05''$ pixel. The corresponding surface brightness is about $12.5 \text{ mag.arcsec}^{-2}$ consistent with the $12.2 \pm 0.5 \text{ mag.arcsec}^{-2}$ measured between $1.1''$ and $1.2''$ (Sect. 2.3.2).

4.4. Summary of model results

Our model involves two dust components:

- a cold annulus peaked at 70 AU from the star made of ISM-like grains in terms of chemical composition (amorphous) and porosity ($P \sim 0.6$) and a very few icy. Assuming a collisional grain size distribution ($\propto a^{-3.5}$), we infer a minimum grain size in the ring of $10 \mu\text{m}$ and we find that bodies as large as at least a few meters may have already been formed. This leads to a total dust mass of a few Earth masses held in a very narrow annulus.
- an inner dust population at about 9–10 AU from the star made of very porous ($P \sim 0.97$) crystalline grains responsible for the emission feature at $\lambda \sim 10 \mu\text{m}$ and for the slight excess centered on the star in the $20.8 \mu\text{m}$ images (Koerner et al., 1998).

5. Implications of the results on the disk dynamics

5.1. Gas to dust ratio

It is of interest to assess the gas to dust ratio in the disk. Given the upper limit on the gas mass $M_g < 1 - 7 M_\oplus$ derived by Greaves et al. (1999) and the dust mass $M_d \simeq 4 M_\oplus$ from model #13 which can be reasonably considered as a lower limit

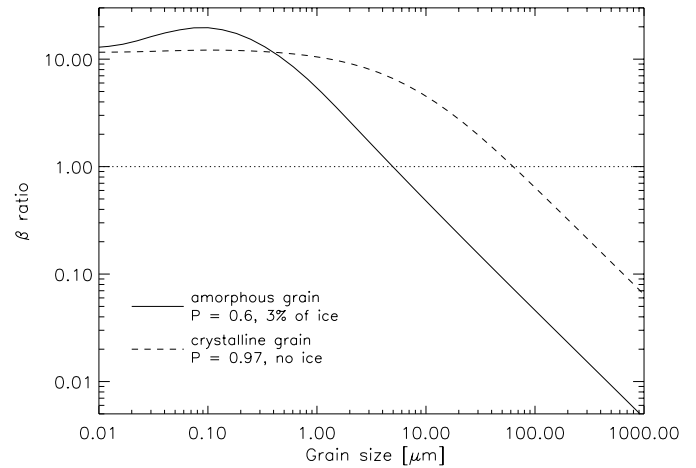


Fig. 13. Radiation pressure force to the gravitational force ratio (β_{pr}) assuming $L_* = 20 L_\odot$ and $M_* = 2.5 M_\odot$. The amorphous grains characterize the cold dust annulus (solid line) and the crystalline ones the hot dust population (dashed line). Below the dotted line, the grains are gravitationally bound.

(see also 5.4.1), we infer a gas to dust ratio less than 1. In this scheme, the gas would probably not play any longer an important role, as claimed by Greaves et al. (1999).

5.2. Radiation pressure

The ratio β_{pr} of radiation pressure to gravity as a function of the grain size is given by:

$$\beta_{\text{pr}} = \frac{3L_* \langle Q_{\text{pr}}(a) \rangle}{16\pi GM_* c a \rho_g} \quad \text{with}$$

$$\langle Q_{\text{pr}}(a) \rangle = \frac{\int Q_{\text{pr}}(a) F_*(\lambda) d\lambda}{\int F_*(\lambda) d\lambda}.$$

assuming $L_* = 20 L_\odot$ and $M_* = 2.5 M_\odot$. We find a blow-out grain size limit ($\beta_{\text{pr}} = 1$) close to $5 \mu\text{m}$ for the amorphous grains in the cold annulus (Fig. 13). Also, amorphous grains with sizes between $10 \mu\text{m}$ ($\beta_{\text{pr}} \simeq 0.5$) and about $45 \mu\text{m}$ ($\beta_{\text{pr}} \simeq 0.1$) have orbits significantly eccentric. Interestingly, the smallest grains we find in our fits in the cold annulus: $a_{\text{min}} \simeq 10 \mu\text{m}$ is very close to the blow-out size limit. For the crystalline grains at 9 AU from the star, the blow-out grain size limit is close to

Table 5. Time-scales under Poynting-Robertson drag, collisions and sublimation. At 70 AU: $\langle a^2 \rangle \simeq 5 a_{\min}^2$, $a_{\text{eq}} \simeq 0.26 \times a$ (model #13) and $T_g \simeq 90$ K (see Fig. 4). At 9 AU: $\sigma_0 \simeq 0.5 \text{ grain.cm}^{-2}$, $\langle a^2 \rangle = a_0^2$ with $a_0 \simeq 450 \mu\text{m}$, $\rho_g = 0.071 \text{ g.cm}^{-3}$ and H_2O ice is sublimated ($a_{\text{eq}} = 0$, see Fig. 5). For both amorphous grains with $a_{\min} = 10 \mu\text{m}$ and crystalline grains with $a_0 \simeq 450 \mu\text{m}$, we find $\langle Q_{\text{abs}} \rangle$ very close to 1.

Dust population	r [AU]	t_{PR} [yr]	t_{coll} [yr]	t_{sub} [yr]
Cold	70	1.7×10^6	1×10^3	2.7×10^5
Hot	9	9×10^4	4×10^2	0

65 μm (Fig. 13). The grains deduced from our modelling are then gravitationally bound.

5.3. Times scales and dominant processes

The life times of the grains in the disk under Poynting-Robertson drag, collisions and sublimation, can be written respectively as (e.g. Backman & Paresce 1993):

$$t_{\text{PR}} = \frac{4\pi c^2}{3} \frac{a \rho_g r^2}{\langle Q_{\text{abs}} \rangle L_*} \simeq 35 \frac{\rho_g}{\langle Q_{\text{abs}} \rangle} a_{\mu\text{m}} r_{\text{AU}}^2 \text{ yr}$$

where $\langle Q_{\text{abs}} \rangle$ is the absorption efficiency averaged over the star spectrum,

$$t_{\text{coll}} \simeq \frac{1}{2\pi \langle a^2 \rangle \sigma(r) \Omega} \simeq \frac{2.5 \times 10^6 r_{\text{AU}}^{\frac{3}{2}}}{\langle a_{\mu\text{m}}^2 \rangle \sigma(r)} \sqrt{\frac{M_{\odot}}{M_*}} \text{ yr}$$

where $\Omega = \sqrt{GM_*/r^3}$ is the Keplerian circular rotation frequency at radius r , and $\langle a^2 \rangle$ the grain size square averaged over the grain size distribution,

$$t_{\text{sub}} = \frac{a_{\text{eq}} \rho_{\text{H}_2\text{O}}}{6.7 \times 10^{11}} \frac{10^{\frac{2480}{T_g}}}{T_g^{3.5}} \simeq 2 \times 10^{-16} a_{\text{eq},\mu\text{m}} \frac{10^{\frac{2480}{T_g}}}{T_g^{3.5}} \text{ yr}$$

where $a_{\text{eq}} = a (P p_{\text{H}_2\text{O}}/100)^{1/3}$ is the equivalent grain radius for a pure ice sphere with the same mass of ice as in a grain with a size a . The time-scales for the cold annulus and the hot dust population are summarized in Table 5.

Collisions are then the dominant process in the cold annulus. The smallest grains produced by collisions in very short time-scales are not efficiently removed from the ring by Poynting-Robertson drag. Only radiation pressure is then able to explain the minimum grain size (10 μm) derived from the SED fitting. Also, this is consistent with the fact that this minimum grain size is very close to the blow-out size limit. Of course, this argument applies only if the gas does not play an important role, as suggested in a previous Sect. (5.1). At 70 AU from the star, the H_2O ice within the smallest grains is sublimated in a short time-scale in comparison with the star age. This is consistent with the little percentage of H_2O ice required to fit the 20–25 μm SED (Sect. 4.2.2).

The hot dust population is poorly constrained; the time-scales in Table 5 have then to be taken with care. The life time

of the 450 μm crystalline grains under Poynting-Robertson drag is long compared to the collision time-scale, and even 120 μm crystalline grains with $\beta_{\text{pr}} \simeq 0.5$ have t_{PR} about 4 times larger than t_{coll} . Also, collisions and radiation pressure are probably the two main processes which shape the hot dust distribution.

5.4. Ring dynamics and confinement

5.4.1. Collision dynamics and mass loss

We here consider the implications of the model parameters for the ring centred at 70 AU given in Table 4. As representative example we consider model #13. This has a total grain surface density $\sigma_0 = 1.79 \times 10^3 \text{ grains.cm}^{-2}$. For the assumed size distribution ($\propto a^{-3.5}$), the mean collision time for the smallest grains with $a = a_{\min} \simeq 10 \mu\text{m}$ is approximately $t_{\text{coll}}(a_{\min}) \simeq 2.1 \times 10^3 \text{ yr}$. As these grains are at the radiation pressure blow out limit and the majority of grains have the minimum size, the minimum mass loss rate is given by:

$$\dot{M} = \frac{M_d(a_{\min})}{t_{\text{coll}}(a_{\min})} = \frac{4\pi a_{\min}^3 \rho_g n(a_{\min})}{3 t_{\text{coll}}(a_{\min})} \sigma_0 A$$

where $A = 1.7 \times 10^{30} \text{ cm}^2$ is the area of the annulus. For model #13 this corresponds to $\dot{M} \simeq 2.5 \times 10^{-6} M_{\oplus} \text{ yr}^{-1}$. Thus the dust mass reservoir required to supply this mass loss over the age of the system is $\sim 20 M_{\oplus}$, which corresponds to a surface density in solids $\Sigma_{\text{gr}} \simeq 0.07 \text{ g.cm}^{-2}$.

It is of interest to note that if we assume a gas to dust ratio of 100 in the primordial nebulae, this corresponds to a surface density $\Sigma \simeq 7 \text{ g.cm}^{-2}$ for the original protostellar disk. This surface density is consistent with that expected at 70 AU for standard disk models corresponding to a minimum mass solar nebula (e.g. Papaloizou & Terquem 1999).

If the surface density Σ_{gr} resides predominantly in objects with $a = a_{\text{max}} \sim 1 \text{ m}$, their collision time would be $t_{\text{coll}} \sim 2a\rho_g/(3\Omega\Sigma_{\text{gr}}) \simeq 8.6 \times 10^4 \text{ yr}$. This is still shorter than the age of the system. With a ring aspect ratio of 0.1 for instance, collisions are expected to occur with a relative velocity $\sim 0.5 \text{ km.s}^{-1}$, and are likely to be destructive. In order to have a collisional lifetime greater than the star age, the objects would have to have a larger than about 100 m. A population of such larger objects providing a mass source for those with $a \sim 1 \text{ m}$, may exist but they would not be detectable. In that case the disk mass could be significantly larger than $4 M_{\oplus}$.

5.4.2. Formation, vertical height and possible presence of larger bodies

In the standard model of planetary formation (Weidenschilling & Cruzzi, 1993), objects in the size range 1 m–1 km are formed by accumulation of smaller objects through collisions when there was still gas present. The presence of gas drag, effective enough here with $\Sigma \sim 7 \text{ g.cm}^{-2}$, would be essential to damp eccentricity and inclination so collisions occur with small relative velocity. However, the collision timescales would be the same as estimated above.

Thus it is reasonable that objects as large as 100 m could be formed if the gas residence time was similar to the present age of the system.

When significant amount of gas was present during earlier phases, the disk would be expected to be thin because of gas drag (Weidenschilling & Cruzzi, 1993) but this could have been thickened due to gravitational perturbations from large external objects. Unfortunately the observations are not yet able to provide constraints on the vertical thickness, but this does not affect the discussion about mass loss rates or collision times because these are independent of the vertical thickness.

5.4.3. Radial confinement

The fact that the mass distribution in the ring is tightly radially confined to a width of about 0.2 times the mean radius, which may be comparable to its vertical thickness, gravitational confinement mechanisms may operate to sculpt its form. As it is likely that many collisions are required to reduce a metre sized object to fragments small enough to be blown out by radiation pressure, if the vertical thickness is as much as $0.2r$, the ring should be significantly wider without a confinement mechanism. Even if the ring is very thin as it might have been immediately post formation so that little collisional spreading occurs, a mechanism is still required to explain why the protostellar gaseous disk was truncated at around 70 AU.

Confinement may occur through gravitational interaction with external perturbers. This situation is familiar in the case of planetary rings (Goldreich & Tremaine, 1982) where the interaction with external orbiting satellites provides confinement. It also occurs for accretion disks in close binary systems where interaction with a binary companion truncates the disk (Papaloizou & Pringle, 1977). The presence of a binary companion in the system discussed here is suggestive that it could play a role in determining the location of the outer boundary to the disk as well as pumping up inclinations after gas dispersal. Note also that an exterior as yet undetected giant planet might provide a similar role.

The binary companion HR 4796 B is seen at a projected distance of 515 AU from the central star whereas the outer disk radius is 70 AU. Thus if it is to play any role in confinement the orbit should be eccentric. As significant interaction with the ring requires the pericentre distance to be less than three times the ring radius, the minimum value for the eccentricity is thus $e = 0.4$, although it could be significantly larger on account of projection effects.

Disk edge truncation can be effective in the presence of binary companions with significant mass ratio in circular or eccentric orbits. In the case of very eccentric orbits, as may well be the case here, the truncation process is most easily modelled as a succession of encounters which occur at each pericentre passage (Ostricker, 1994; Korycansky & Papaloizou, 1995; Hall, 1997). From these studies it is clear that in order to be truncated, the disk radius should initially exceed about one third of pericentre distance. Material beyond this radius is strongly perturbed and removed from the disk which devel-

ops a truncated edge there. The latter phenomenon, which occurs because of angular momentum transported from the disk to the companion, was seen in the gas disk simulations of Korycansky & Papaloizou (1995) and the free particle simulations of Hall (1997) and is also expected for the disks of the type considered here.

6. Conclusion

We propose a two dust population model able to reproduce all the available observations of the HR 4796 A circumstellar disk. The first dust population, peaked at 70 AU from the star, shapes like a narrow annulus. Its small radial extension suggests a gravitational confinement mechanism both outside and inside the peak at 70 AU. This ring is made of amorphous grains quite similar to those found in the interstellar medium. Under the assumption of a collisional grain size distribution, grains larger than $10 \mu\text{m}$ to meter sized bodies are required to fit the data. Collisions, occurring in short time scales, are expected to produce smallest grains down to the blow out size limit ($\sim 10 \mu\text{m}$). This conclusion applies because of the gas to dust ratio smaller than 1 inferred. The second dust population at 9-10 AU from the star is made of comet-like grains. Higher signal to noise ratio measurements and resolved images at $\lambda \sim 10 \mu\text{m}$ would allow to better constrain this dust population (spatial extension, grain size range) and its dynamics.

The dust surrounding HR 4796 A probably shows an intermediate stage for the circumstellar matter between pre-main sequence stars and evolved ones like β Pictoris, Fomalhaut, Vega, 55 Cnc ... The presence of a companion (HR 4796 B) is also an interesting peculiarity among the Vega-like stars. As a large number of field stars are members of binary (or more) systems, HR 4796 A does not represent a marginal case. Therefore, the dynamics of the disk has to be further studied, in terms of chemical evolution of the grains and dust distribution to better understand the steps which lead or not to planetary systems formation.

Acknowledgements. We wish to thank G. Schneider and J.S. Greaves for providing data prior to publication and S. Warren for providing water ice optical constants. We also thank Hervé Beust for helpful discussions on the dynamics of the system. All the computations presented in this paper were performed at the Service Commun de Calcul Intensif de l'Observatoire de Grenoble (SCCI).

References

- Artymowicz P., Burrows C., Paresce F., 1989, ApJ 337, 494
- Artymowicz P., Lubow S.H., 1994, ApJ 421, 651
- Backman D., Gillett F.C., Witterborn F.C., 1992, ApJ 385, 670
- Backman D., Paresce F., 1993, In: Levy, Lunine (eds.) Protostars and Planets III, University of Arizona Press, Tucson, p. 1253
- Bertie J., Labbe H., Walley E., 1969, J. Chem. Phys. vol. 50, 4501
- Bohren C.F., Huffman D.R., 1983, Absorption and scattering of light by small particles. Wiley, New York
- Draine B.T., Lee H.M., 1984, ApJ 285, 89
- Draine B.T., 1985, ApJS 57, 587
- Fajardo-Acosta S.B., Telesco C.M., Knacke R.F., 1998, AJ 115, 2101
- Fink, Sill, 1982, In: Comets. U. Arizona Press

- Goldreich P., Tremaine S., 1982, *ARA&A* 20, 294
- Greaves J.S., Mannings V., Holland, 1999, *Icarus*, submitted
- Greenberg J.M., Yencha A.J., Corbett J.W., Frisch H.L., 1972, *Mem. Soc. Roy. des sciences de Liege*, 6e Serie, tome IV, p. 425
- Greenberg J.M., 1986, In: Israel F. (ed.) *Light on Dark Matter*. Reidel, Dordrecht, p. 177
- Greenberg J.M., Hage J.I., 1990, *ApJ* 361, 260
- Greenberg J.M., 1998, *A&A* 330, 375
- Hall S.M., 1997, *MNRAS* 287, 148
- Hellyer B., 1970, *MNRAS* 148, 383
- Heney L.G., Greenstein J.L., 1941, *ApJ* 93, 70
- Hudgins D.M., Sandford S.A., Allamandola L.J., Tielens A.G.G.M., 1993, *ApJS* 86, 713
- Jayawardhana R., Fisher S., Hartmann L., et al., 1998, *ApJ*, 503, L79
- Jura M., Zuckerman B., Becklin E.E., Smith R.C., 1993, *ApJ* 418, L37
- Jura M., Ghez A.M., White R.J., et al., 1995, *ApJ* 445, 451
- Jura M., Malkan M., White R.J., et al., 1998, *ApJ* 505, 897
- Kalas P., Jewitt D., 1993, *BAAS* 25, 1353
- Koerner D.W., Ressler M.E., Werner M.W., Backman D.E., 1998, *ApJ* 503, L83
- Korycansky D.G., Papaloizou J.C.B., 1995, *ApJS* 105, 181
- Laor A., Draine B.T., 1993, *ApJ* 402, 441
- Lecavelier des Etangs A., Vidal-Madjar A., Ferlet R., 1996, *A&A* 307, 542
- Li A., Greenberg J.M., 1997, *A&A* 323, 566
- Li A., Greenberg J.M., 1998, *A&A* 331, 291
- Mathis J.S., 1996, *ApJ* 472, 643
- Mathis J.S., Whiffen G., 1989, *ApJ* 341, 808
- Mathis J.S., Rimpl W., Nordsieck K.H., 1977, *ApJ* 217, 425
- Mouillet D., Lagrange A.M., Beuzit J.-L., Renaud N., 1997a, *A&A* 324, 1083
- Mukai T., Koike C., 1990, *Icarus* 87, 180
- Nakano T., 1990, *ApJ* 355, L43
- Ockman N., 1958, *Adv. Phys.* vol. 7, 199
- Ostricker E.C., 1994, *ApJ* 424, 292
- Pantin E., Lagage P.-O., Artymowicz P., 1997, *A&A* 327, 1123
- Papaloizou J.C.B., Pringle J.E., 1977, *MNRAS* 181, 441
- Papaloizou J.C.B., Terquem C., 1999, *ApJ*, in press
- Pollack J.B., Hollenbach D., Beckwith S., et al., 1994, *ApJ* 421, 615
- Schneider G., Smith B.A., Becklin E.E., et al., 1999, *ApJ* 513, L127
- Stauffer J.R., Hartmann L.W., Barrado y Navascues D., 1995, *ApJ* 454, 910
- Warren, S., 1984, *Appl. Opt.* 23, 1206
- Weidenschilling S.J., Cruzzi J.N., 1993, In: Levy, Lunine (eds.) *Proto-stars and Planets III*, University of Arizona Press, Tucson, p. 1031